Holographic Nano-Imaging of Terahertz Dirac Plasmon Polaritons in Topological Insulator Antenna Resonators

*Valentino Pistore, Leonardo Viti, Chiara Schiattarella, Zhengtianye Wang, Stephanie Law, Oleg Mitrofanov, and Miriam S. Vitiello**

Excitation of Dirac plasmon polaritons (DPPs) in bi-dimensional materials have attracted considerable interest in recent years, both from perspectives of understanding their physics and exploring their transformative potential for nanophotonic devices, including ultra-sensitive plasmonic sensors, ultrafast saturable absorbers, modulators, and switches. Topological insulators (TIs) represent an ideal technological platform in this respect because they can support plasmon polaritons formed by Dirac carriers in the topological surface states. Tracing propagation of DPPs is a very challenging task, particularly at terahertz (THz) frequencies, where the DPP wavelength becomes over one order of magnitude shorter than the free space photon wavelength. Furthermore, severe attenuation hinders the comprehensive analysis of their characteristics. Here, the properties of DPPs in real TI-based devices are revealed. Bi_2Se_3 rectangular antennas can efficiently confine the propagation of DPPs to a single dimension and, as a result, enhance the DPPs visibility despite the strong intrinsic attenuation. The plasmon dispersion and loss properties from plasmon profiles are experimentally determined, along the antennas, obtained using holographic near-field nano-imaging in a wide range of THz frequencies, from 2.05 to 4.3 THz. The detailed investigation of the unveiled DPP properties can guide the design of novel topological quantum devices exploiting their directional propagation.

1. Introduction

Topological insulators (TIs) are a class of quantum materials comprising insulating bulk and conducting surface states, named topological surface states (TSSs) residing in the topological bandgap.[1–3] Owing to the non-trivial topology of the band structure, charge carriers in TSSs are protected from backscattering on defects and disorder.[1–3] Charge carriers in these states can participate in collective excitations at the TI surface – the Dirac plasmon polaritons (DPPs)[4] surface-phonon-plasmon polariton modes,[5–6] promising applications in areas of quantum information,[7] spintronics,[8] terahertz (THz) photonics[9] and laser physics.[10] DPPs in TIs have attracted considerable interest in recent years,[11–16] and experimental studies at THz frequencies have proven instrumental in gaining insights into the physics of DPPs and in determining their properties [4,13]. However, the experimental characterization of DPPs is

V. Pistore, L. Viti, C. Schiattarella, M. S. Vitiello
NEST
CNR-Istituto Nanoscienze and Scuola Normale Superiore
Piazza San Silvestro 12, Pisa 56127, Italy
E-mail: miriam.vitiello@sns.it
Z. Wang
Department of Materials Science and Engineering
University of Delaware
Newark, DE 19716, USA

S. Law
Materials Science and Engineering
Pennsylvania State University
University Park, PA 16802, USA

O. Mitrofanov
University College London
Electronic and Electrical Engineering
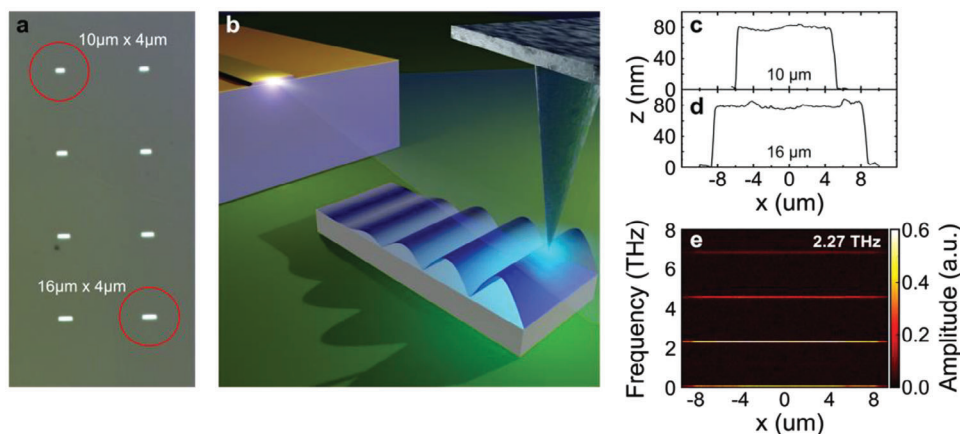London WC1E 7JE, UK

Figure 1. a) Optical image of the Bi_2Se_3 antennas fabricated on a sapphire substrate. The two antennas marked with red circles are investigated in this work. b) Artistic representation of the THz Dirac plasmon polaritons (DPPs), in blue, launched by the AFM probe of the s-SNOM system illuminated by a THz QCL. c) AFM topographic line profile of the 10 μm antenna marked in the top left corner of a. d) AFM topographic line profile of the 16 μm antenna marked in the bottom right corner of a. e) SFMX signal amplitude map recorded from the 16 μm long antenna at 2.27 THz.

not trivial. The conductivity of typically grown TIs, such as bismuth and antimony chalcogenides, in fact contains contributions from the bulk carriers due to doping from antisite defects and Se and Te vacancies,[17] as well as a 2D electron gas (2DEG) of massive carriers, which can arise in a thin volume within 20 nm from the surface, due to band bending.[18] These charge carriers also support plasmon polaritons, but they lack the topological protections of TSSs and display lower mobilities and shorter scattering lifetimes affecting DPPs properties[19]. Experimental characterization of DPPs in TIs therefore is critical.

The difficulty arises since the DPP wavelength in TIs is about one order of magnitude shorter than the free space photon wavelength.[4,12] THz scattering-type scanning near-field optical microscopy (s-SNOM) was recently applied to probe DPPs in exfoliated TI flakes[20] and epitaxially-grown uniform layers.[21] s-SNOM confirmed the deeply subwavelength nature of plasmon polaritons and provided insight into relative contributions of the Dirac, 2DEG, and bulk carriers.[20,21] However, s-SNOM experiments also revealed an additional challenge: strong attenuation experienced by DPPs suppresses their amplitude within approximately one oscillation,[20] inevitably leading to a large uncertainty in determining the DPPs characteristics.

Here we show that rectangular antennas offer an effective solution for investigating the properties of plasmons in TIs in the THz range, mitigating the strong DPPs damping observed in previous studies.[20,21] Lithographically defined antenna geometry can confine the propagation of DPPs to a single dimension, avoiding the fast dissipation of DPPs due to the radial divergence of s-SNOM tip-launched waves.[21] We fabricated dipolar antennas made of Bi_2Se_3, and characterized plasmons traveling along the antennas. To cover a spectral range (from 2 up to 4.3 THz), where the plasmon dispersion is affected by phonon resonances, at 1.92 and 4.05 THz[22], we use quantum cascade lasers (QCLs)[23–25] as both sources and detectors, by exploiting the self-mixing (SFMX) effect in the QCL cavity.[26–32] To enhance the contrast due to plasmons, we adopt a recently developed technique, synthetic holographic THz nano-imaging, which is capable of spatial mapping the plasmon phase.[20,21,33] As a result, the

experimentally observed surface plasmons display complete field oscillations along the plasmon propagation path, allowing us to determine the plasmon wavevector. Furthermore, we show that the s-SNOM signal within the TI antenna resonators is dominated by DPPs launched by the s-SNOM tip, rather than by DPPs excited directly by the incident beam. This experimental approach, in principle applicable to other layered material systems with strong plasmon damping, is hence ideal for unveiling the DPPs properties.

2. Results

In the present work, we investigate Bi_2Se_3, a prototypical material of choice for studying the TIs properties. In fact, the TSSs in this material present a single Dirac cone on the surface,[34] protected by the Z_2 topological invariant of the bulk,[1] and are characterized by helical behavior[35] and strong spin-orbit coupling.[2] We fabricated antennas using an epitaxially grown 80 nm thick layer of Bi_2Se_3 on sapphire (see Experimental Section).

Figure 1a shows an optical image of the Bi_2Se_3 antenna sample. Two antennas, 10 and 16 μm long and 4 μm wide, were selected for these investigations (circled). Figure 1c shows the antenna topography measured by atomic force microscopy (AFM).

The choice of antenna parameters was determined by the properties of the DPPs waves and by the nature of s-SNOM signal collected from the Bi_2Se_3 antennas. In our setup, schematically represented in Figure S1 (Supporting Information), THz radiation is generated by a QCL, driven in continuous wave (CW) (see Experimental Section), and focused on the s-SNOM probe. The incident THz waves are then concentrated by the probe apex on the Bi_2Se_3 surface to launch DPPs, which propagate isotropically away from the tip as a cylindrical surface wave. The narrow (4 μm) width of the antenna prevents radial dissipation of the DPP energy, confining its propagation within one dimension and therefore enabling better visibility of DPPs. Upon reaching the antenna ends, DPPs are reflected back to the AFM tip, which then scatters the plasmon to the far-field.[36] We detect the scattered wave using the SFMX voltage change read directly
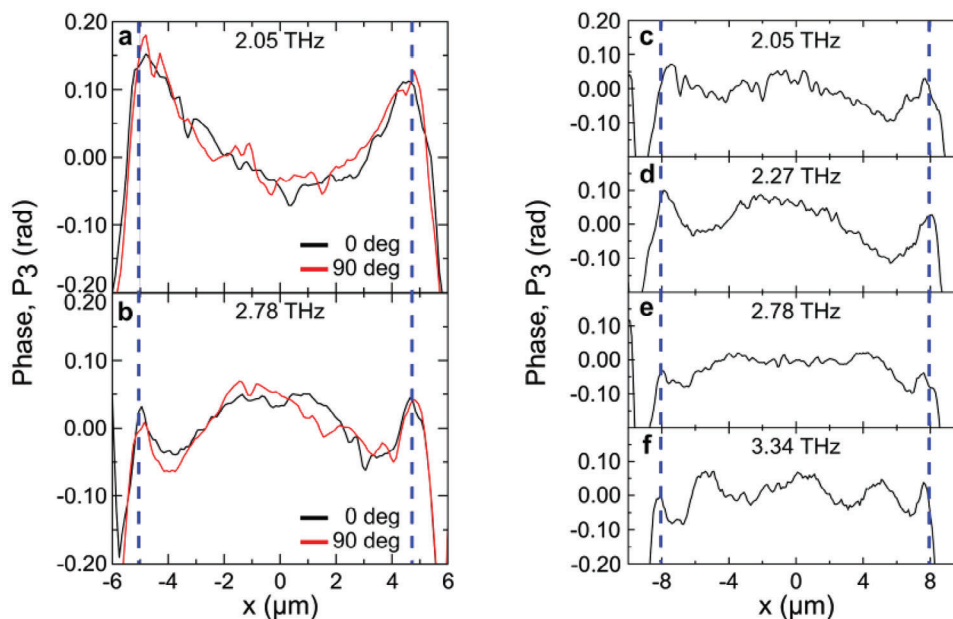
Figure 2. a,b) Phase profiles at 2.05 a) and at 2.78 THz b) along the 10 μm antenna. The signal is demodulated at the third harmonic of the tapping frequency (P_3). Black traces were measured with the antenna oriented in the plane of incidence and red traces were measured for the antenna perpendicular to it. c–f) Phase profile P_3 was measured along the 16 μm antenna at 2.05 c), at 2.27 d), at 2.78 e), and at 3.34 THz f) respectively.

from the QCL.[29] An illustration of the DPP waves launched by the AFM probe is shown in Figure 1b.

The s-SNOM signal also contains a component due to surface polarization by the tip. Its contribution to the SFMX signal depends on the sample dielectric permittivity near the tip and therefore it represents local material properties. Finally, the p-polarized incident THz wave can also excite DPPs on the antenna directly by polarizing it.[38] However, as we show later, the corresponding s-SNOM signal is negligible. Consequently, the total s-SNOM signal from the Bi_2Se_3 antenna is primarily a superposition of the material component and the DPPs launched by the tip.

To determine the plasmon polariton dispersion properties, we performed synthetic digital near-field holography[38] in a compact detector-less configuration.[29] We acquired profiles of the s-SNOM signal along the antenna length by iteratively scanning the AFM tip over the same path with a 100 nm sampling step. At the beginning of each scan, we changed the path length between the QCL and the AFM tip and thus recorded an SFMX interferogram consisting of 256 line-scans with varying positions of the delay stage (every 4 μm), which effectively modifies the phase of the scattered field. By applying a Fourier transform to the interferogram, we therefore can obtain the amplitude and phase spectra of the s-SNOM signal for every point along the antenna.[39] The phase information is key for isolating the DPPs contribution to the scattered signal.

The amplitude spectrum of the SFMX signal, measured along the 16 μm-long antenna illuminated with a 2.27 THz QCL is illustrated in Figure 1d. It clearly shows the fundamental frequency of the QCL, as well as the two higher-order harmonics at 4.54 and 6.81 THz, commonly observed in the SFMX signal.[33] The spectrum independently provides the QCL emission frequency for each measurement. The spatial profile also shows that the

s-SNOM signal is ≈2 times stronger when the tip is over the Bi_2Se_3 area, in comparison to the sapphire substrate.

In addition to the scattered signal amplitude profile (Figure 1d), the Fourier transform provides the signal phase. **Figure 2** shows the measured SFMX phase along the 10 μm antenna at two different frequencies, 2.05 THz (Figure 2a) and 2.78 THz (Figure 2b). The signal was demodulated at the third harmonic of the tapping frequency (denoted as P_3). The phase profiles consistently show visible oscillations, similar to the fringes recently observed near large-area Bi_2Se_3 edges and ascribed to DPPs[21], and indicate the formation of tip-launched DPPs along the antennas. Amplitude profiles also show oscillations with the same periodicity as the phase profiles (as shown in the Supporting Information), however, we found that the phase profiles provide more accurate and reliable k-vector values in comparison to the amplitude profiles, and therefore, to achieve higher accuracy, we used the phase of s-SNOM signal for determining the parameters of DPPs in this work.

Remarkably, the profiles display mirror symmetry with respect to the antenna center, in contrast to the typically antisymmetric profiles observed in s-SNOM studies of THz plasmonic resonators.[40] To confirm this observation, we recorded phase profiles along the antennas oriented in the plane of incidence (red profiles) and orthogonal to it (black profiles). The absence of any significant difference between these profiles confirms that antenna resonances, which can form on the antenna oriented in the plane of incidence by the p-polarized light, play a negligible role in our measurements. This allows us to study DPPs profiles without the need of accounting for directly excited antenna resonances, as our system only shows sensitivity to the DPPs launched by the tip. Furthermore, any antenna orientation can be used in these measurements.
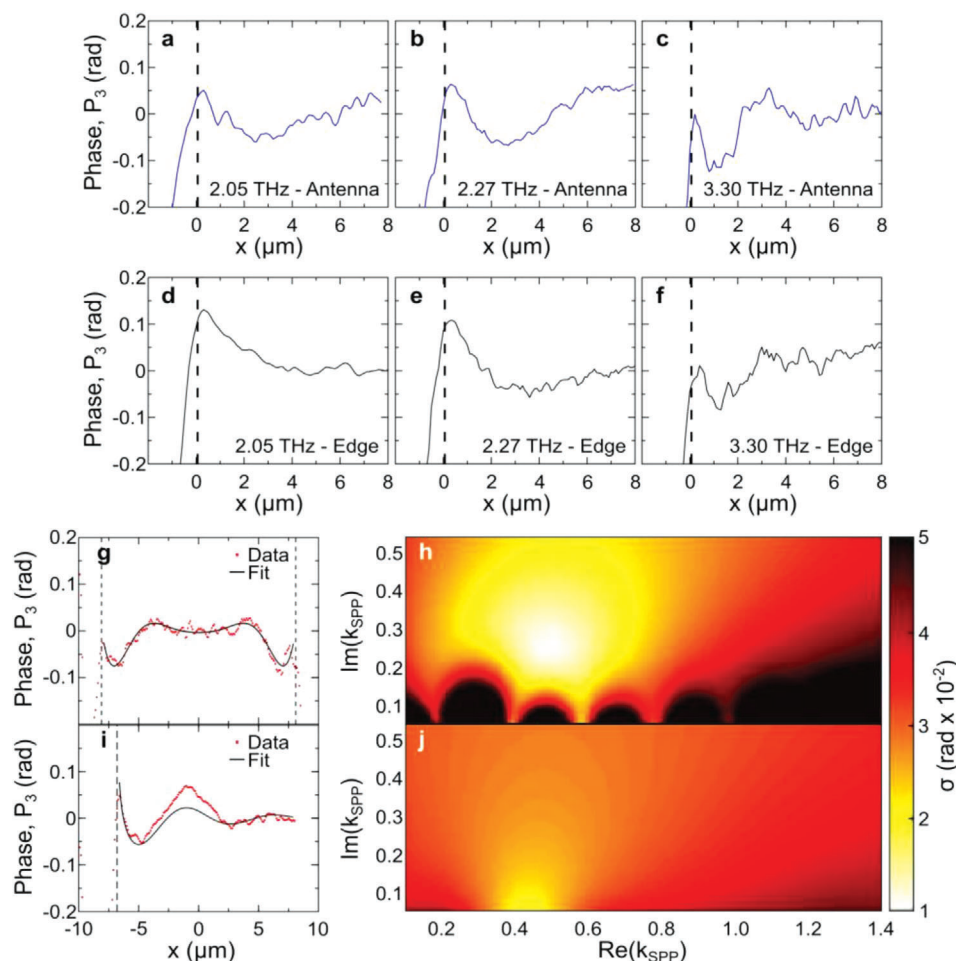
ADVANCED
SCIENCE NEWS
www.advancedsciencenews.com

NANO · MICRO
small
www.small-journal.com

Figure 3. a–c) Phase profiles P_3 along the 16 µm antenna (averaging procedure is described in the Supporting Information). d–f) Phase profiles P_3 measured across the edge of Bi_2Se_3 square. g) Phase profile P_3 along the 16 µm antenna described by the model (black line), and the experimental data (red symbols). Dashed lines mark the antenna edges h) Map of the standard deviation of the phase profile fit along the 16 µm antenna, for different combinations of the real and imaginary part of the surface plasmon polariton (SPP) wavevector. i) Phase profile P_3 across the Bi_2Se_3 edge described by the model (black line) and the data (red symbols). j) Standard deviation of the phase profile fit along the large-area Bi_2Se_3 layer, for different combinations of the real and imaginary part of the SPP wavevector. In the colormap of panels h and j, the brighter the color, the lower the fitting error. Hence a brighter and smaller spot is indicative of a better fitting.

The profile at the lowest frequency (2.05 THz) shows two maxima at the edges and a single minimum at the center of the 10 µm antenna (Figure 2b). It indicates that the DPP wavelength in this case is larger or comparable to the antenna length, making quantitative analysis challenging. Therefore, we perform further tests on the 16 µm long antenna, which is long enough to display complete oscillations of the phase along the antenna. The recorded phase profiles are shown in Figure 2c–f at 2.05, 2.23, 2.78, and 3.34 THz, respectively. At least one complete phase oscillation is now visible, even at 2.05 THz. At higher frequencies, the oscillations are more frequent, showing as many as 4 cycles at 3.34 THz.

Next, we compare the phase profiles recorded on the 16 µm antenna (**Figure 3a–c**) with those measured under the same experimental conditions at an edge of a large Bi_2Se_3 square fabricated on the same sample (Figure 3d–f). In the latter case, the phase variation near the edge often diminishes on the scale comparable to or shorter than the oscillation period seen for the antenna.

In particular, the phase profile at the edge measured at 2.05 THz (Figure 3d) does not develop clear oscillations, but rather a gradual decay. This is a consequence of the strong attenuation of surface plasmons combined with the 2D geometrical divergence occurring near a wide edge.[21] In comparison, the DPPs decay is not as severe in the quasi-1D antenna case.

The antenna geometry is the most effective solution in confining DPPs and increases the accuracy of determining the k-vector (see Figure 3). While indeed more conventional stripe geometries (as ribbons) could also support DDPs, the energy of the DDPs is expected to be strongly spread out along the ribbon itself, meaning that ribbons would show poor accuracy in determining the k-vector.

3. Discussion

The uncertainty in determining the plasmon k-vector from the experiment can be reduced for the antenna geometry in
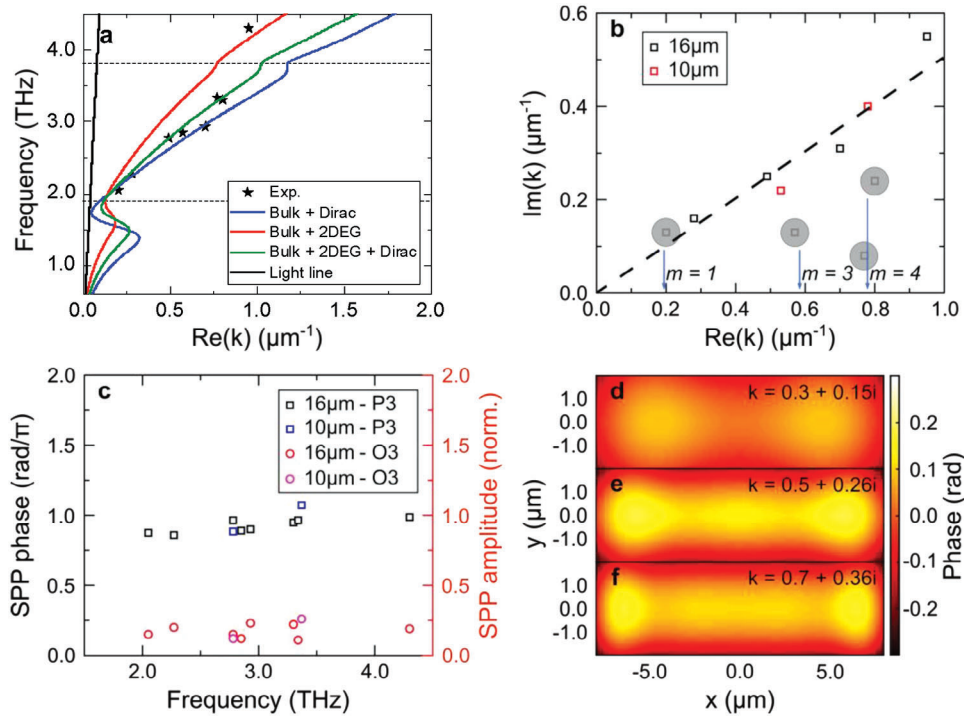
Figure 4. a) Dispersion of surface plasmon polaritons in Bi$_2$Se$_3$ as obtained by fitting of phase (P3) profiles along antennas (symbols). Colored solid lines show dispersion calculations based on the analytical conductivity model and include the contributions of bulk carriers, Dirac carriers, and massive surface carriers (2DEG). The optical phonon contribution to the conductivity is included for each model. b) Imaginary part versus real part of the DPPs wavevector at the QCL frequencies. The circled points highlight the results for the k-vectors closely matching the multiples of the inverse antenna length. c) Tip-launched plasmon amplitude (circles) and offset phase (squares) at the QCL frequencies. d–f) s-SNOM phase signal on the 16 µm antenna predicted by our model at k-vectors of 0.3 + 0.15i µm^{-1} d), 0.5 + 0.26i µm^{-1} e), and 0.7 + 0.36i µm^{-1} f).

comparison to the edge. Although the physical mechanisms for generation and detection of DPPs are identical for the two cases,[21] the lateral confinement of plasmons within the antenna can improve the visibility of the interference pattern along the antenna formed by the tip-launched DPPs.

To quantify the k-vector, we model the s-SNOM signal using the mechanism of tip-launched DPPs.[21] DPPs originate from the tip, propagate to the antenna edges, reflect from the edges, and finally return back to the tip, which scatters the DPP back to the QCL.[20] In the antenna case, the lateral confinement can be approximated simply by assuming the guided (1D) plasmon propagation along the antenna. Therefore, in the DPPs description, we include only the exponential decay. In contrast, the DPP field amplitude near the edge of a uniform layer is a product of the DPPs exponential decay and a $(2r)^{-1/2}$ function representing the divergence of DPPs launched at a distance r from the edge. The s-SNOM signal from the tip-launched DPP along the antenna structure can be expressed as follows:

$$E_p(x) = A \left(e^{i2k_p\left(x+\frac{L}{2}\right)} + e^{-i2k_p\left(x-\frac{L}{2}\right)} \right) + A_+(y) + A_-(y) \qquad (1)$$

Each term of the expression represents one of the primary DDP waves reflected from each side of the antenna and contributing to the s-SNOM signal: two counterpropagating DPPs traveling along the antenna axis (x), and two counterpropagating DPPs traveling perpendicular to the antenna axis (denoted as A_+

and A_-). A is the complex amplitude of the DPPs, k_p is the complex wavevector, L is the antenna length and $x = 0$ represents the antenna center.

The model describes the observed amplitude and phase profiles along the antennas with good accuracy. In particular, it reproduces the oscillating features at the antenna ends with the mirror symmetry and gradual attenuation of the oscillations toward the antenna center (see Figure 3g). By fitting a model-defined function to the data, we can now determine the real and imaginary parts of the plasmon wave vector k. To select the best fit, we calculated the standard deviation σ for all values of the k-vector and displayed the result as a map in Figure 3h. A clear minimum in the map allows us to determine a combination of Re{k} and Im{k} values that describe the DPP waves for each QCL frequency. The fitting procedure is described in Section S4 (Supporting Information).

For comparison, fitting profiles observed near the square edge with the model introduced in Ref. [21] do not always converge to a reasonable combination of Re{k} and Im{k} values, as it is illustrated in Figure 3i,j. Although the fitting procedure finds an optimal value of Re{k}, the model does not converge to an optimal Im{k} value. We attribute this to the 2D nature of the tip-launched plasma waves near the wide edge: the plasma wave amplitude drops quickly, limiting the accuracy of experimentally obtained k-vector values.

Figure 4a summarizes the extracted Re{k} values for all QCL frequencies: the momentum increases monotonically with the

QCL frequency, with an inflection point close to the A_{2u} phonon frequency. These dispersion measurements provide an insight into the origin of plasmons by comparing the observations with predictions of analytical conductivity models.[21,41] Dispersion results for the analytical models are plotted in Figure 4 for comparison. We find that the observed plasmons follow the dispersion given by a combination of bulk, Dirac, and massive surface carriers. The best agreement is given by $n_{Bulk} = 3.6 \times 10^{18}$ cm^{-3}, $n_{Dirac} = 1.2 \times 10^{13}$ cm^{-2} and $n_{2DEG} = 4 \times 10^{12}$ cm^{-2}, where the Dirac carriers provide the main contribution. Further details are given in the Supporting Information.

Having confirmed the origin of plasmons in our samples, we can now evaluate the losses that they experience as they travel along antennas. The question of DPP loss is central in developing practical TI-enabled devices, and for Bi$_2$Se$_3$ applications in the THz range, this question is especially critical due to the presence of phonons[42] and due to unknown losses that can occur at the resonator edges. The map in Figure 3i reveals the Im{k} value that gives the best match to the DPPs on an antenna, and in Figure 4b we summarize Im{k} values against Re{k} for all QCL frequencies. The imaginary part increases with the real part, and most points in the range from 2.05 to 4.3 THz follow practically a linear dependence.

The physical meaning of the ratio Re{k}/Im{k} is the relative attenuation length of plasmon: Re{k}/(2π Im{k}) = L_p /λ_p, where L_p is the amplitude decay length and λ_p is the plasmon wavelength. The linear dependence trend in Figure 4b indicates that the relative attenuation length for plasmons supported by our Bi$_2$Se$_3$ antenna remains constant L_p /λ_p, ≈ 0.3. The plasmon amplitude decays within $\approx 1/3$ of the plasmon wavelength, a length shorter than that found in Ref. [21] for tip-launched THz plasmons on uniform layers of Bi$_2$Se$_3$. We attribute this fast decay to additional losses experienced by plasmons at the edges of the antenna, as the experimentally found value represents the attenuation length within the antenna, rather than on a uniform surface.

Most data points lay close to the line defined as Im{k} = 0.51 Re{k}. However, other data points fall clearly below this line (circled points in Figure 4b). We find that these points correspond to Re{k} values closely matching a multiple of the inverse length of the antenna, hence corresponding to antenna resonance conditions $k_m = m\pi$ L^{-1}, where m is the integer and L is the antenna length. The plasmon reflection from the antenna edges therefore interferes constructively, resulting in lower fitted Im{k} values. If the antenna length is changed, however, fitted Im{k} values return to the linear trend, as shown in Figure 4b for the 10 μm length antenna (red symbols). We note that at 2.05 THz the fitted Im{k} value was found to be higher than expected from the linear trend. We attribute this to the presence of a phonon, which increases losses near the phonon resonance.[42] We also note that the polaritonic pattern is more visible in the antenna geometry than on uniform layers of Bi$_2$Se$_3$, regardless of the presence of Fabry–Perot resonances. When such resonances are excited, PP propagation losses appear to be artificially smaller (Figure 4b).

Finally, the entire set of experiments allows us to extract the complex amplitude of the tip-launched plasmons. This parameter is essential for describing the s-SNOM signal and it represents a combination of several physical processes: launching, reflection from an edge, and scattering. In the fitting process, we set the complex amplitude to be a free parameter, and in

Figure 4c we show the amplitude and phase values that give the lowest fitting error for all profiles. The plasmon amplitude is normalized to that for the scattered signal over Bi$_2$Se$_3$, and we found it to be ≈ 0.2, independent of the QCL frequency. The phase of the plasmon signal (relative to the phase of s-SNOM signal on uniform Bi$_2$Se$_3$) is also nearly constant at a value of π. The consistency in the extracted complex amplitude values across the broad range of QCL frequencies indicates that the mathematical model describes the observations with good accuracy.

We can now fully describe the expected s-SNOM signal on the antenna surface. First, we used the plasmon parameters extracted from the 16 μm antenna profiles to predict DPPs profiles for the 10 μm antenna (see Section S5, Supporting Information). The model displays very good matching with the measured profiles, supporting the model's effectiveness. More generally, we can predict an s-SNOM phase map on the entire antenna surface. Three prototypical examples of phase distribution on the antenna are displayed in Figure 4d–f for k-vectors of 0.3+0.15i μm^{-1} (Figure 4d), 0.5+0.26i μm^{-1} (Figure 4e), and 0.7+0.36i μm^{-1} (Figure 4f). One can notice that the two strongest maxima are always observed close to the antenna edges, whereas the oscillations in the middle of the antenna appear to be more dampened for increasing frequencies.

In conclusion, we investigated DPPs on rectangular antennas made of Bi$_2$Se$_3$ and showed that the antenna geometry provides an effective platform for determining plasmon dispersion properties in TIs in the THz range. It mitigates the strong DPPs damping observed in previous studies.[20,21] This approach allowed us to determine the Dirac plasmon-polariton dispersion properties in a wide spectral range (from 2.05 up to 4.3 THz), where the plasmon dispersion is affected by phonons and residual carriers (bulk and 2DEG). The possibility of capturing purely DPPs, launched by the s-SNOM tip in lithographically defined structures, open intriguing opportunities in THz nanoplasmonics and topological nanophotonics. Enhancing the DPPs visibility, as shown here, is only one application. Future promising THz applications include the development of integrated devices for confining the THz radiation to deeply subwavelength volumes, and THz metasurfaces with subwavelength meta-atoms.

4. Experimental Section

MBE Growth of Bi$_2$Se$_3$:   The Bi$_2$Se$_3$ large-area (≈ 1 cm^2) film was grown using a Veeco GENxplor molecular beam epitaxy system on an as-shipped epi-ready 10 mm × 10 mm × 0.5 mm c-plane sapphire substrate. The substrate was first baked in a load lock (pressure < 10^{-7} Torr) at 200 °C for 12 h and then transferred to the growth chamber (system base pressure < 10^{-9} Torr). Prior to the growth, the substrate was further degassed by heating to 650 °C with a 20 °C min^{-1} ramp rate and held at 650 °C for 5 min. The substrate temperature was measured via a non-contact thermocouple. The substrate was then cooled to 325 °C. The Bi$_2$Se$_3$ thin film was grown via a two-step method:[43] a 4 nm Bi$_2$Se$_3$ seed layer was first deposited at 325 °C and then annealed at 425 °C for 20 min; the remaining 76 nm of the film was then deposited at 425 °C using co-deposition with a growth rate of 0.6 nm min^{-1}. Selenium was supplied using a cracker source, while bismuth was supplied using a dual-filament source. After the deposition was complete, the film was cooled to 200 °C under a selenium flux and transferred out of the growth chamber once the substrate temperature dropped below 200 °C. The film was then vacuum-sealed for storage before further processing.

Fabrication of the Bi₂Se₃ Nanoantennas: The antenna arrays were fabricated using a standard e-beam lithography process established in the University of Delaware Nanofabrication Facility (UDNF): ≈300 nm of the negative e-beam resist AR-N 7520.18 (Allresist, DE) was spin-coated on the sample, followed by immediate e-beam exposure (100 kV) with a Raith EBPG5200 system. The resist was developed by dipping the sample in developer AR 300–47 (4:1 diluted, Allresist, DE) for 90s, followed by a DI water rinse and nitrogen blow drying. Then the film was dry etched with an argon plasma using an Intlvac Nanoquest ion mill etcher. The approximate etching rate was 1 nm sec^{-1}. After etching, the films were immediately transferred to a solution of N-Methyl-2-pyrrolidone (NMP) in a water bath at 80 °C for half an hour to remove the resist. After nanofabrication, the sample was vacuum-sealed for storage before further optical measurement.

Bi₂Se₃ Dispersion: Here, a Bi₂Se₃ thin film was modeled as a 2D conductive slab of zero thickness, a commonly used approximation,[21,41] which was proven valid for 2D materials with a layer thickness much smaller than the polariton wavelength. This approximation does not require calculating the fields inside the slab. The slab conductivity (σ_{bulk}) is given by the relation $\sigma_{bulk} = \epsilon_{bulk} \cdot (c \cdot d / 2i\lambda_0)$, where ϵ_{bulk} is the TI permittivity, c is the speed of light, d is the slab thickness and λ_0 is the free-space wavelength, thus taking into account the layer thickness. Here, ϵ_{bulk} includes the contributions of bulk carriers and transverse optical (TO) phonons E$_u$ ($\omega_{to}^{\perp}$ = 63.03 cm^{-1}) and A$_{2u}$ ($\omega_{to}^{//}$ = 126.94 cm^{-1}), involving atomic vibrations in the plane orthogonal ($\perp$) and parallel (//) to the trigonal c-axis, respectively.[22] The TO phonon frequencies are marked by dashed lines in Figure 4a. The total TI conductivity was then obtained by summing σ_{bulk} to the conductivities given by the other carrier types present in the TI layer: Dirac carriers (σ_{DC}) and massive surface carriers (σ_{2DEG}), see Supporting Information for further details.

Detectorless s-SNOM: QCLs were cryogenically cooled in a helium-flow cryostat (Janis technologies) at a fixed temperature of 15K (depending on the specific QCL employed, the signal-to-noise ratio on the SFMX signal depends on the heat-sink temperature). THz light was collected and collimated by a parabolic mirror in front of the QCL, brought through an optical delay-line and then focused onto the atomic force microscope (AFM) probe tip (40 nm radius, RMN300B-40 from Rocky Mountains) as a *p*-polarized wave by a second parabolic mirror integrated to the s-SNOM (NeaSNOM from NeaSpec/Attocube). The fraction of laser radiation backscattered from the tip-sample system was then coupled back into the QCL cavity along the same optical path, giving rise to a voltage response on the QCL (SFMX voltage) whose amplitude and phase depend on the THz field scattered by the tip.[29]

Supporting Information

Supporting Information is available from the Wiley Online Library or from the author.

Acknowledgements

Conflict of Interest

The authors declare no conflict of interest.

Data Availability Statement

The data that support the findings of this study are available from the corresponding author upon reasonable request.

[1] C. L. Kane, E. J. Mele, *Phys. Rev. Lett.* **2005**, *95*, 146802.

[2] J. E. Moore, L. Balents, *Phys. Rev. B* **2007**, *75*, 121306.

[3] M. Z. Hasan, C. L. Kane, *Rev. Mod. Phys.* **2010**, *82*, 3045.

[4] P. Di Pietro, M. Ortolani, O. Limaj, A. Di Gaspare, V. Giliberti, F. Giorgianni, M. Brahlek, N. Bansal, N. Koirala, S. Oh, P. Calvani, S. Lupi, *Nat. Nanotechnol.* **2013**, *8*, 556.

[5] M. A. Huber, F. Mooshammer, M. Plankl, L. Viti, F. Sandner, L. Z. Kastner, T. Frank, J. Fabian, M. S. Vitiello, T. L. Cocker, R. Huber, *Nat. Nanotechnol.* **2017**, *12*, 207.

[6] V. W. Brar, M. S. Jang, M. Sherrott, S. Kim, J. J. Lopez, L. B. Kim, M. Choi, H. Atwater, *Nano Lett.* **2014**, *14*, 3876.

[7] M. He, H. Sun, Q. L. He, *Front. Phys.* **2019**, *14*, 43401.

[8] Q. L. He, T. L. Hughes, N. P. Armitage, Y. Tokura, K. L. Wang, *Nat. Mater.* **2022**, *21*, 15.

[9] F. Giorgianni, E. Chiadroni, A. Rovere, M. Cestelli-Guidi, A. Perucchi, M. Bellaveglia, M. Castellano, D. Di Giovenale, G. Di Pirro, M. Ferrario, R. Pompili, C. Vaccarezza, F. Villa, A. Cianchi, A. Mostacci, M. Petrarca, M. Brahlek, N. Koirala, S. Oh, S. Lupi, *Nat. Commun.* **2016**, *7*, 11421.

[10] P. Yan, R. Lin, S. Ruan, A. Liu, H. Chen, Y. Zheng, S. Chen, C. Guo, J. Hu, *Sci. Rep.* **2015**, *5*, 8690.

[11] A. Karch, *Phys. Rev. B* **2011**, *83*, 245432.

[12] M. Autore, P. Di Pietro, A. Di Gaspare, F. D'apuzzo, F. Giorgianni, M. Brahlek, N. Koirala, S. Oh, S. Lupi, *J Phys Condens Matter* **2017**, *29*, 183002.

[13] L. L. Hale, Z. Wang, C. T. Harris, I. Brener, S. Law, O. Mitrofanov, *APL Photonics* **2023**, *8*, 051304.

[14] C. In, S. Sim, B. Kim, H. Bae, H. Jung, W. Jang, M. Son, J. Moon, M. Salehi, S. Y. Seo, A. Soon, M.-H. Ham, H. Lee, S. Oh, D. Kim, M.-H. Jo, H. Choi, *Nano Lett.* **2018**, *18*, 734.

[15] P. Di Pietro, N. Adhlakha, F. Piccirilli, A. Di Gaspare, J. Moon, S. Oh, S. Di Mitri, S. Spampinati, A. Perucchi, S. Lupi, *Phys. Rev. Lett.* **2020**, *124*, 226403.

[16] C. In, U. J. Kim, H. Choi, *Light Sci Appl* **2022**, *11*, 313.

[17] M. Brahlek, Y. S. Kim, N. Bansal, E. Edrey, S. Oh, *Appl. Phys. Lett.* **2011**, *99*, 012109.

[18] M. Bianchi, D. Guan, S. Bao, J. Mi, B. B. Iversen, P. D. C. King, P. Hofmann, *Nat. Commun.* **2010**, *1*, 128.

[19] V. S. Kamboj, A. Singh, T. Ferrus, H. E. Beere, L. B. Duffy, T. Hesjedal, C. H. W. Barnes, D. A. Ritchie, *ACS Photonics* **2017**, *4*, 2711.

[20] E. A. A. Pogna, L. Viti, A. Politano, M. Brambilla, G. Scamarcio, M. S. Vitiello, *Nat. Commun.* **2021**, *12*, 6672.

[21] S. Chen, A. Bylinkin, Z. Wang, M. Schnell, G. Chandan, P. Li, A. Y. Nikitin, S. Law, R. Hillenbrand, *Nat. Commun.* **2022**, *13*, 1374.

[22] S. V. Dordevic, M. S. Wolf, N. Stojilovic, H. Lei, C. Petrovic, *J. Phys.: Condens. Matter* **2013**, *25*, 075501.

[23] J. Faist, F. Capasso, D. L. Sivco, C. Sirtori, A. L. Hutchinson, A. Y. Cho, *Science* **1994**, *264*, 553.

[24] R. Köhler, A. Tredicucci, F. Beltram, H. E. Beere, E. H. Linfield, A. G. Davies, D. A. Ritchie, R. C. Iotti, F. Rossi, *Nature* **2002**, *417*, 156.

[25] M. S. Vitiello, P. De Natale, *Adv. Quantum Technol.* **2022**, *5*, 2100082.

[26] P. Dean, Y. Leng Lim, A. Valavanis, R. Kliese, M. Nikolic, S. P. Khanna, M. Lachab, D. Indjin, Z. Ikonic, P. Harrison, A. D. Rakic, E. H. Linfield, A. G. Davies, *Opt. Lett.* **2011**, *36*, 2587.

[27] F. P. Mezzapesa, L. L. Columbo, M. Brambilla, M. Dabbicco, M. S. Vitiello, G. Scamarcio, *Appl. Phys. Lett.* **2014**, *104*, 041112.

[28] F. P. Mezzapesa, M. Petruzzella, M. Dabbicco, H. E. Beere, D. A. Ritchie, M. S. Vitiello, G. Scamarcio, *IEEE Trans Terahertz Sci Technol* **2014**, *4*, 631.

[29] M. C. Giordano, S. Mastel, C. Liewald, L. L. Columbo, M. Brambilla, L. Viti, A. Politano, K. Zhang, L. Li, A. G. Davies, E. H. Linfield, R. Hillenbrand, F. Keilmann, G. Scamarcio, M. S. Vitiello, *Opt Express* **2018**, *26*, 18423.

[30] E. A. A. Pogna, M. Asgari, V. Zannier, L. Sorba, L. Viti, M. S. Vitiello, *Light Sci Appl* **2020**, *9*, 189.

[31] K. S. Reichel, E. A. A. Pogna, S. Biasco, L. Viti, A. Di Gaspare, H. E. Beere, D. A. Ritchie, M. S. Vitiello, *Nanophotonics* **2021**, *10*, 1495.

[32] E. A. A. Pogna, C. Silvestri, L. L. Columbo, M. Brambilla, G. Scamarcio, M. S. Vitiello, *APL Photonics* **2021**, *6*, 061302.

[33] V. Pistore, E. A. A. Pogna, L. Viti, L. Li, A. G. Davies, E. H. Linfield, M. S. Vitiello, *Adv. Sci.* **2022**, *9*, 2270181.

[34] Y. Xia, D. Qian, D. Hsieh, L. Wray, A. Pal, H. Lin, A. Bansil, D. Grauer, Y. S. Hor, R. J. Cava, M. Z. Hasan, *Nat. Phys.* **2009**, *5*, 398.

[35] C.-X. Liu, X.-L. Qi, H. Zhang, X. Dai, Z. Fang, S.-C. Zhang, *Phys. Rev. B* **2010**, *82*, 045122.

[36] F. Keilmann, R. Hillenbrand, *Philos Trans A Math Phys Eng Sci* **2004**, *362*, 787.

[37] R. Mueckstein, C. Graham, C. C. Renaud, A. J. Seeds, J. A. Harrington, O. Mitrofanov, *J. Infrared, Millimeter, Terahertz Waves* **2011**, *32*, 1031.

[38] C. Chen, S. Chen, R. P. S. M. Lobo, C. Maciel-Escudero, M. Lewin, T. Taubner, W. Xiong, M. Xu, X. Zhang, X. Miao, P. Li, R. Hillenbrand, *ACS Photonics* **2020**, *7*, 3499.

[39] M. Schnell, P. S. Carney, R. Hillenbrand, *Nat. Commun.* **2014**, *5*, 3499.

[40] N. Sulollari, J. Keeley, S. Park, P. Rubino, A. D. Burnett, L. Li, M. C. Rosamond, E. H. Linfield, A. G. Davies, J. E. Cunningham, P. Dean, *APL Photonics* **2021**, *6*, 066104.

[41] F. J. Alfaro-Mozaz, S. G. Rodrigo, P. Alonso-González, S. Vélez, I. Dolado, F. Casanova, L. E. Hueso, L. Martín-Moreno, R. Hillenbrand, A. Y. Nikitin, *Nat. Commun.* **2019**, *10*, 42.

[42] Y. Deshko, L. Krusin-Elbaum, V. Menon, A. Khanikaev, J. Trevino, *Opt. Express* **2016**, *24*, 7398.

[43] Z. Wang, S. Law, *Cryst. Growth Des.* **2021**, *21*, 6752.

2308116 (8 of 8)